Radiative cooling and atmospheric perturbation effects of dust aerosol from the Aralkum Desert in Central Asia

Jamie R. Banks[1], Bernd Heinold[1], and Kerstin Schepanski[2]

[1]Leibniz Institute for Tropospheric Research (TROPOS), Leipzig, Germany.
[2]Institute of Meteorology, Freie Universität Berlin, Berlin, Germany.

Correspondence: Jamie R. Banks (banks@tropos.de)

Abstract.

The Aralkum is a new desert created by the desiccation of the Aral Sea since the 1960s, and is an efficient source of dust aerosol which may perturb the regional Central Asian radiation balance. COSMO-MUSCAT model simulations are used to quantify the direct radiative effects (DREs) of Aralkum dust, and investigate the associated perturbations to the atmospheric environment. Considering scenarios of 'Past' and 'Present' defined by differences in surface water coverage, it is found that in the Present scenario the yearly mean net surface DRE across the Aralkum is $-1.34\pm6.19\,\mathrm{W\,m^{-2}}$, of which $-0.15\pm1.19\,\mathrm{W\,m^{-2}}$ comes from dust emitted by the Aralkum. Meanwhile in the atmosphere the yearly mean DRE is $-0.62\pm2.91\,\mathrm{W\,m^{-2}}$, of which $-0.05\pm0.51\,\mathrm{W\,m^{-2}}$ comes from Aralkum dust: on the yearly timescale Aralkum dust is cooling both at the surface and in the atmosphere. The daytime surface cooling effect (solar zenith angle $\lesssim70\text{-}80°$) outweighs both the nighttime heating effect and the corresponding atmospheric daytime (solar zenith angle $\lesssim60\text{-}70°$) heating and nighttime cooling effects. Instantaneous Aralkum dust DREs contribute up to $-116\,\mathrm{W\,m^{-2}}$ of surface cooling and $+54\,\mathrm{W\,m^{-2}}$ of atmospheric heating. Aralkum dust perturbs the surface pressure in the vicinity of the Aralkum by up to $+0.76\,\mathrm{Pa}$ on the monthly timescale, implying a strengthening of the Siberian High in winter and a weakening of the Central Asian Heat Low in summer.

1 Introduction

The formation of the Aralkum (the Aral Desert, Breckle and Wucherer (2012)) due to the desiccation of the Aral Sea over the last 60 years (Micklin, 2010) has generated a new source of atmospheric dust aerosol in Central Asia (e.g. Groll et al., 2013; Nobakht et al., 2021, and others). The Aral Sea is supplied by water from the Amu Darya and Syr Darya rivers (originating in the Pamir and Tian Shan mountains), however since the 1960s the water from these rivers has been exploited more extensively for irrigation, which has resulted in a dramatic reduction in the outflow to the Aral Sea. Approximately $60,000\,\mathrm{km^2}$ or $\sim90\%$ of the former lakebed has been exposed by this desiccation, revealing an erodible surface efficient at emitting dust into the atmosphere given favourable wind conditions. Among other impacts, this has had particularly negative consequences for air quality and human health in the region, exacerbated by the pesticide and fertiliser chemicals in the Aralkum's soils associated with the irrigation practices which created its desert (e.g. O'Hara et al., 2000; Wiggs et al., 2003, and others).

Figure 1. Map of Central Asia, marking its countries, deserts and water bodies, overlaid on the NASA 'Blue Marble' image. The orange box encompasses the Aralkum. Relevant major Central Asian weather patterns are named (as described on p. 14 of Global Facility for Disaster Risk Reduction and Recovery (2019)), with arrows indicating their flow regimes and colours indicative of their temperature regimes.

It is well known that an environmental impact of dust aerosol is on the Earth's radiation balance, in terms of both solar and
25 thermal radiation (e.g. Hsu et al., 2000; Banks et al., 2014; Alamirew et al., 2018, and others), and so it is to be expected that dust from the Aralkum would add an extra perturbation to the Earth's radiation environment. With respect to shortwave (SW) solar radiation, in its optical properties dust is highly scattering but also partially absorbing (e.g. Haywood et al., 2003; Ryder et al., 2013, and others), with the effect that during daylight hours lofted dust aerosol tends to cool the surface underneath it, but warms the atmospheric layer in which it is located. The longwave (LW) thermal direct radiative effect (DRE) of dust is
30 more complex, and relates not only to the optical properties of the dust but also to the atmospheric temperature and moisture profiles, and to the altitude and vertical distribution of the dust layer (e.g. Haywood et al., 2005; Brindley and Russell, 2009, and others). In hot and cloud-free desert environments, in terms of LW radiation dust is likely to have a warming effect on the surface beneath, since it traps LW radiation being emitted by the surface, as well as absorbing incoming SW radiation from above. The behaviour of the LW DRE is more complicated at night, during winter, and over more diverse non-desert
35 environments such as are also present in Central Asia. The net (SW+LW) radiative effect of dust can therefore be cooling or warming, depending on the altitude of the dust within the atmosphere, the time-of-day, the season, the surface albedo, and the precise mineralogy and optical properties of the dust.

This paper builds on the Central Asian dust modelling study presented in Banks et al. (2022), henceforth denoted BHS22, to explore the consequences of Aralkum dust for radiative effects over Central Asia. BHS22 presented regional model simulations
40 of dust emissions and transport from the deserts of Central Asia and specifically from the Aralkum under three scenarios of Aral Sea water coverage, considering the 'Past' (end of 20th century), the 'Present' (beginning of 21st century), and an Aralkum lakebed-only scenario as a sensitivity study. The concept of the Present scenario is to produce as accurately as possible a current

representation of the dust emissions and transport from all the Central Asian dust sources with the inclusion of the Aralkum. Meanwhile the concept of the Past scenario is to depict the state of the dust environment as it was three to four decades ago (including dust from the pre-existing deserts of the Karakum and the Kyzylkum in Turkmenistan and Uzbekistan), when the Aral Sea was much more extensive than it is today. The Aralkum-only scenario is a less physical case, an idealised scenario which excludes the other Central Asian deserts so as to investigate the atmospheric dust concentrations of dust exclusively from the Aralkum. Over the course of a 1-year case study simulation period, it was found that there has been a near-doubling in dust emissions from the Aralkum region (43-47°N, 58-62°E, including non-lakebed surfaces) between the Past and the Present due to the expansion of the Aralkum. In terms of air quality, settlements as far as ~600-800 km downwind to the east of the Aralkum may be badly affected by its dust. It is also clear that there is a high degree of interannual variability in the directions of the dust-emitting winds over the Aralkum, such that in other years other directions are more susceptible to Aralkum dust. Problematically for observations of the Aralkum's dust, approximately two-thirds of the Aralkum's dust emissions are simulated to occur under cloudy skies, and hence would be impossible to observe with traditional passive remote sensing techniques. Open questions remain, however, as to the dust radiative effects: what may be the consequences of the changes in Aralkum dust activity for the radiative effects of dust over the region? What are the patterns of radiative cooling and warming on the surface and atmosphere of the Aralkum region, can these be quantified, and how have these changed as the Aral Sea has shrunk and the Aralkum has expanded? Moreover, have these radiative effects had consequences for the wider atmospheric environment of the region?

In order to explore these questions as to the radiative effects of Aralkum dust, this paper takes the following structure: in Section 2 we describe the COSMO-MUSCAT model setup used to simulate regional dust emissions and transport, and dust's influence on the regional SW and LW radiative fluxes; in Section 3 we explore the behaviour and patterns of dust radiative effects over the Aralkum; in Section 4 we consider the changes in the radiative effects due to growing dust emissions from the Aralkum (i.e. the difference between 'Past' and 'Present'); and finally in Section 5 we consider perturbations to the atmospheric state due to the presence of Aralkum dust in the atmosphere.

2 The COSMO-MUSCAT model, the DUBLT scenarios, and the model configuration of dust radiative effects

2.1 COSMO-MUSCAT, the 'Dustbelt' domain, and dust emission

The regional aerosol model COSMO-MUSCAT (COSMO: COnsortium for Small-scale MOdelling; MUSCAT: MUltiScale Chemistry Aerosol Transport Model) is based on version 5.05 of the atmospheric model COSMO (Schättler et al., 2014), which is coupled online with the chemistry tracer transport model MUSCAT (Wolke et al., 2012). Mineral dust is an aerosol species which may be modelled using COSMO-MUSCAT, simulating dust transport processes including emission and dry and wet deposition, thereby providing 3D dust atmospheric concentrations (Heinold et al., 2011). Dust radiative effects are also simulated (see Section 2.2).

The Central Asian domain is contained within the 'Dustbelt' ('DUBLT') modelling domain (BHS22), which spans the deserts of North Africa, the Middle East, and Central Asia. The DUBLT domain is projected onto a rectangular rotated pole

grid with an origin at 20°N, 45°E (in Saudi Arabia), and with a domain size of 160 latitudinal grid cells by 360 longitudinal grid cells. The grid spacing is 0.25° (28 km), which produces a domain that extends as far north as ∼50°N in Kazakhstan and as far east as ∼84°E in China. For the purposes of the current study, focusing on the radiative effects of dust from the Aralkum and its neighbouring deserts, the Central Asian component of the model domain is considered to be bounded by 35-49°N,
80 48-72°E.

The parameterisation of dust emission follows the saltation bombardment scheme of Marticorena and Bergametti (1995), a formulation which for given soil properties and wind speeds calculates first the horizontal saltation flux G, which has a linear relationship with the vertical emission flux F. The sandblasting efficiency α, dependent on the soil size distribution, is the coefficient of proportionality between F and G. Soil properties are described by version 2.0 of the SoilGrids250m
85 dataset (Hengl et al., 2017; Poggio et al., 2021), although missing data within the former Aral Sea basin are filled in with measurements made by Argaman et al. (2006) of soils in the southern Aralkum. The roughness length z_0 is described by retrievals from ASCAT and PARASOL data performed by Prigent et al. (2012); missing z_0 data within the Aralkum are filled in using the minimum value from the vicinity of the basin, which for the Aralkum is 0.02 cm. Dust emission is suppressed in the presence of vegetation and snow (both derived from Aqua MODIS retrievals (Didan, 2015; Hall and Riggs, 2016)), such
90 that:

$$F = \alpha * (1 - A_{\text{snow}}) * A_{\text{eff}} * A_{\text{land}} * G, \tag{1}$$

where A_{eff} is the 'effective' bare and unvegetated surface area fraction, and A_{snow} and A_{land} are the snow and land area fractions.

The DUBLT modelling system has been developed in order to evaluate the effects of changes in surface water coverage on dust emissions and transport (BHS22). It does this by making use of the Global Surface Water dataset (Pekel et al., 2016), which
95 makes use of aggregated Landsat data during the periods 1984-1999 (interpreted within DUBLT as the 'Past') and 2000-2015 (the 'Present'), and which is publicly available at https://global-surface-water.appspot.com/ (last accessed 11th July 2023). The dataset has subsequently been updated to extend to 2020. For more extensive information on the DUBLT modelling system and its output in terms of dust emission and transport, see BHS22.

2.2 Model configuration of dust and radiation

100 Within COSMO-MUSCAT dust is considered to be a passive tracer, with five independent size bins (j) with radii bounded by 0.1 and 24.0 μm. The effective radii of these bins have values $r_{\text{eff}} = (0.169, 0.501, 1.514, 4.570, 13.80)\,\mu$m. The dust shape assumption is spherical, and the particles are assumed to have the density of quartz, 2.65 g cm^{-3}. Dust radiative feedbacks are switched on so as to include the effects of dust on the atmospheric dynamics (Helmert et al., 2007). With respect to the calculation of the dust aerosol optical depth (DOD) at 550 nm, the dust refractive indices are defined as described by Sinyuk
105 et al. (2003). Since the simulated dust particles are spherical Mie Theory (Mie, 1908) can be used to calculate the extinction efficiencies Q_{ext}: for the five size bins $Q_{\text{ext}} = (1.677, 3.179, 2.356, 2.144, 2.071)$. The DODs are then obtained by multiplying

the height-resolved (k) dust concentrations $c_{\text{dust}}(j,k)$ by $Q_{\text{ext}}(j)$ and integrating over the atmospheric column:

$$DOD = \sum_{j} \sum_{k} \left(\frac{3}{4} \frac{Q_{\text{ext}}(j)}{r_{\text{eff}}(j)\rho_{\text{p}}} c_{\text{dust}}(j,k)\Delta z(k) \right), \tag{2}$$

where ρ_{p} is the particle density and $\Delta z(k)$ is the thickness of each atmospheric layer.

110   Atmospheric radiation fluxes are modelled via eight spectral bands (Helmert et al., 2007): three of these bands comprise the SW broadband which covers the spectral range of 0.25-4.64 μm, while the other five spectral bands comprise the LW, which covers the range 4.64-104.5 μm. Radiative transfer is computed using the radiation scheme described by Ritter and Geleyn (1992), deploying a δ-two-stream radiative transfer solver approach. The impact of dust on the radiation fluxes across the SW and LW bands is simulated using refractive indices collected and described by Helmert et al. (2007).

115   Dust direct radiative effects (DRE) in the SW and LW are computed with reference to the DUBLT_NODUST scenario, which is a COSMO-MUSCAT run without any dust emissions and hence with atmospheric dust concentrations set to zero. Within the model the convention is that radiative fluxes are positive in the downwards direction, and hence positive net surface (SFC) fluxes SW_{SFC} and LW_{SFC} imply a net warming of the surface. Similarly, positive values of the top-of-the-atmosphere (TOA) net fluxes imply a net warming of the Earth-atmosphere system. COSMO-MUSCAT provides both SFC and TOA net

120   fluxes as model output. In the SW, the surface DRE ($DRE_{\text{SW,SFC}}$) is therefore defined as:

$$DRE_{\text{SW,SFC}} = SW_{\text{SFC,DUST}} - SW_{\text{SFC,NODUST}}. \tag{3}$$

The same equation holds for the LW and for the TOA fluxes. From the difference between the TOA and the SFC DREs, it is straightforward to isolate the atmosphere-only (ATM) DREs:

$$DRE_{\text{SW,ATM}} = DRE_{\text{SW,TOA}} - DRE_{\text{SW,SFC}}. \tag{4}$$

125   In order to exclude the substantial confounding effects of cloud and to identify the dust-only radiative effects, DRE calculations are only performed up to a fairly stringent maximum of 1% cloud cover in both of the DUST and NODUST simulations. Throughout this paper it is important to recall that at a longitude of ∼60°E, the local time over the Aralkum is approximately four hours ahead of UTC.

When considering dust radiative effects on the surface and on the atmosphere, the surface albedo is essential background

130   information, maps of which are presented for the first days of six months during the DUBLT simulation year in Fig. 2. MODIS (Moderate Resolution Imaging Spectroradiometer) albedo retrievals are used for this purpose within the COSMO-MUSCAT simulations, albeit modified by surface snow and ice generated within the COSMO simulations. Snow and ice are particularly noticeable at the beginning of April, December and February over the north of the domain in Kazakhstan, as well as over the Tian Shan and Pamir mountains, and also over the modelled lake surface of the Aral Sea especially in February. In contrast

135   during the late spring and the summer and autumn months, the albedo of the lake of the Aral Sea is distinctly lower than that of its surroundings. It is therefore to be expected that the simulated radiative effects of dust directly over the Aral Sea will be strongly dependent on the season in which it is emitted, and on the simulated freezing state of the lake.
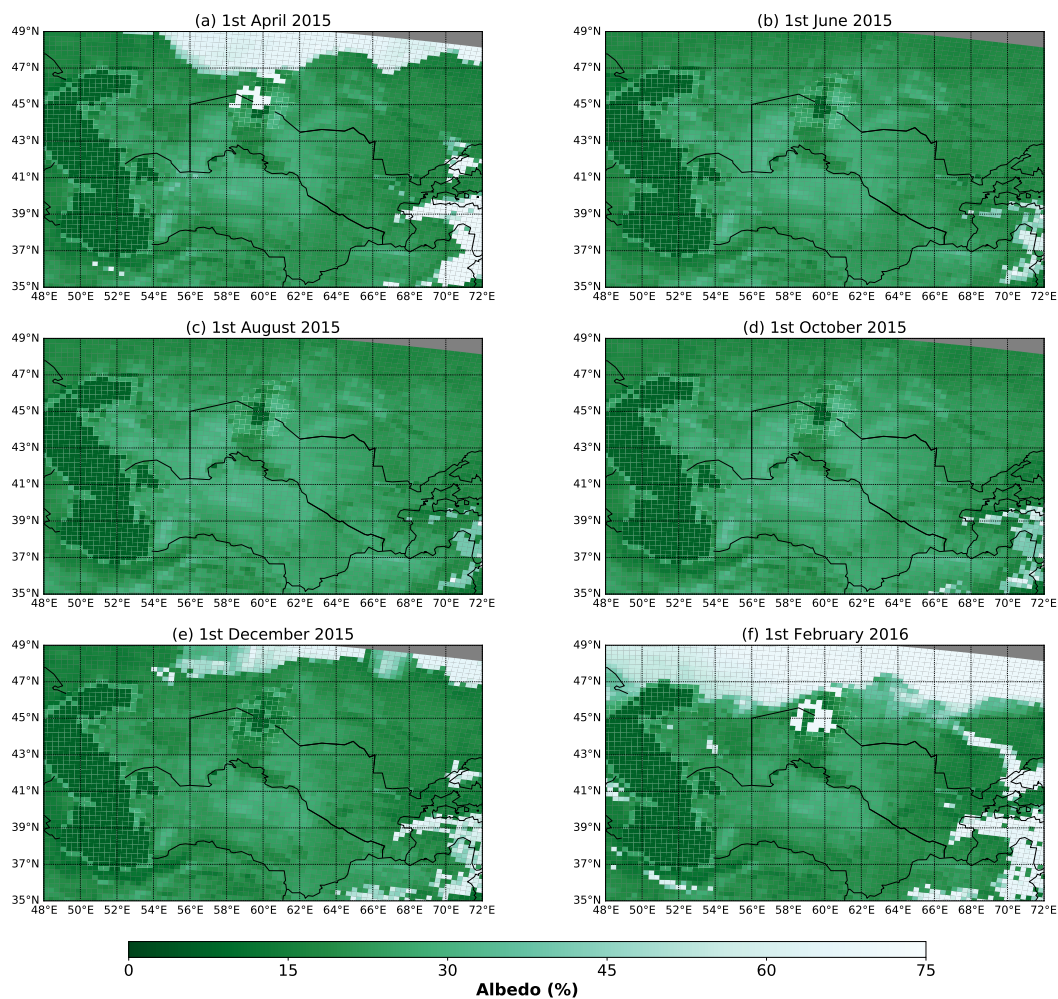
Figure 2. Monthly maps of surface albedo (%) over Central Asia, from 0900 UTC on 1st of each month. Grey areas to the north lie outside of the DUBLT domain. Within the Aralkum (43-47°N, 58-62°E) the mean albedo is (a) 29.5%, (b) 22.7%, (c) 23.5%, (d) 23.5%, (e) 19.1%, and (f) 34.3%.

Within COSMO-MUSCAT there are multiple possibilities as to the assumption of the dust optical properties. Within this paper, we make use of a dust type derived by Helmert et al. (2007), which is considered to be a 'reflecting' (i.e. scattering) dust type. This reflecting dust is aggregated from three dust optical properties databases within wavelength ranges from 0.25-0.44 μm (Sinyuk et al., 2003), 0.44-1.02 μm (Dubovik et al., 2002), 1.02-2.52 μm (Sokolik and Toon, 1999), and 2.52-35.19 μm (Volz, 1973). At IR wavelengths > 35.19 μm, the refractive indices are set to be constant at the 35.19 μm values. These dust optical properties were derived from remote sensing observations, in-situ retrievals at Cape Verde, laboratory measurements, and bulk sampling, respectively. The reflecting dust is currently regarded as the default dust type in COSMO-MUSCAT, and was also the dust type assumed in BHS22.

Within the context of this study, there are three dust model scenarios: 1) the baseline DUBLT scenario, representative of 'Present' surface water coverage and hence Present dust emissions (also known as 'DUBLT_PRESENT'); 2) DUBLT_PAST, representative of Past dust emissions; and 3) DUBLT_NODUST, a simulation run without dust emissions so as to provide information about the atmospheric state in the absence of dust. The first two scenarios were presented and described in BHS22.

150 The simulation period is 30th March 2015 - 29th March 2016, with a two-week model spinup period beforehand to initialise the dust concentrations.

2.3 Quantification of the uncertainties in the COSMO-MUSCAT radiative fluxes

In order to ascertain the uncertainties in the simulated radiative fluxes over the Aralkum, before we can even consider the effects of dust, Fig. 3 compares the DUBLT simulated TOA fluxes with those retrieved from the CERES (Clouds and the Earth's Radiant Energy System) instrument onboard NASA's Aqua and Terra satellites (Wielicki et al., 1996; Loeb et al., 2001;

155 Doelling et al., 2013). These CERES TOA flux data are the Level 3 SSF1deg (Single Scanner Footprint) Aqua data, which are daily mean values spatially averaged onto a uniform $1°$ grid. The CERES SW band is in the spectral range 0.3-5 μm, and the LW band is from 5-200 μm (Loeb et al., 2016), note that these are different from the COSMO-MUSCAT bands of 0.25-4.64 and 4.64-104.5 μm as mentioned previously in Section 2.2. Given the well-understood seasonal cycle in the atmospheric fluxes,

160 it is to be expected that the overall correlations between the simulated and the retrieved fluxes are very close to 1, slightly better simulated in the SW than the LW. The net TOA fluxes switch from positive to negative approximately at the beginning of September, and return to being positive later in March. In general the DUBLT fluxes are biased high, up to +8.5 $\mathrm{W\,m^{-2}}$ in the SW, +1.9 $\mathrm{W\,m^{-2}}$ in the LW and +10.4 $\mathrm{W\,m^{-2}}$ for the net fluxes. Most importantly, considering the RMSDs as an estimate of the uncertainties on the DUBLT simulated fluxes, this uncertainty on the SW fluxes would therefore be $\pm9.7\,\mathrm{W\,m^{-2}}$ while

165 that for the LW is lower at $\pm5.6\,\mathrm{W\,m^{-2}}$; cumulatively this gives an uncertainty on the net fluxes of $\pm13.1\,\mathrm{W\,m^{-2}}$. For further information as to the performance of the DUBLT modelling scheme in simulating regional dust loadings, see Section 4.1 in BHS22.

3 Overview of the dust direct radiative effects in the Aralkum region during the DUBLT year

For an overview of the Aralkum's dust activity over the year, Fig. 4 depicts the cloud-screened timeseries of the Aralkum's

170 dust emissions, DODs and dust DREs during the course of the year, separately for the approximate midday and midnight timeslots (0900 and 2100 UTC). The data are cloud-screened so as only to consider those timeslots when DRE calculations are successfully performed. The timeseries of the emissions and DODs (panels (a-d)) show the extent to which dust activity is event-based, with high DODs occurring only occasionally: notable daytime peaks occur in winter and March 2016, while notable nighttime peaks are in autumn and later in the winter. Due to strict cloud-screening there are gaps in the timeseries

175 (especially in winter), and so a number of dust events are not depicted in this timeseries as a result of being coincident with cloud cover. The co-location of cloud coverage and dust emissions was discussed in detail in BHS22, which found that over two-thirds of the simulated yearly emissions occurred under extensive cloud cover, including the two days in March 2016 (15th
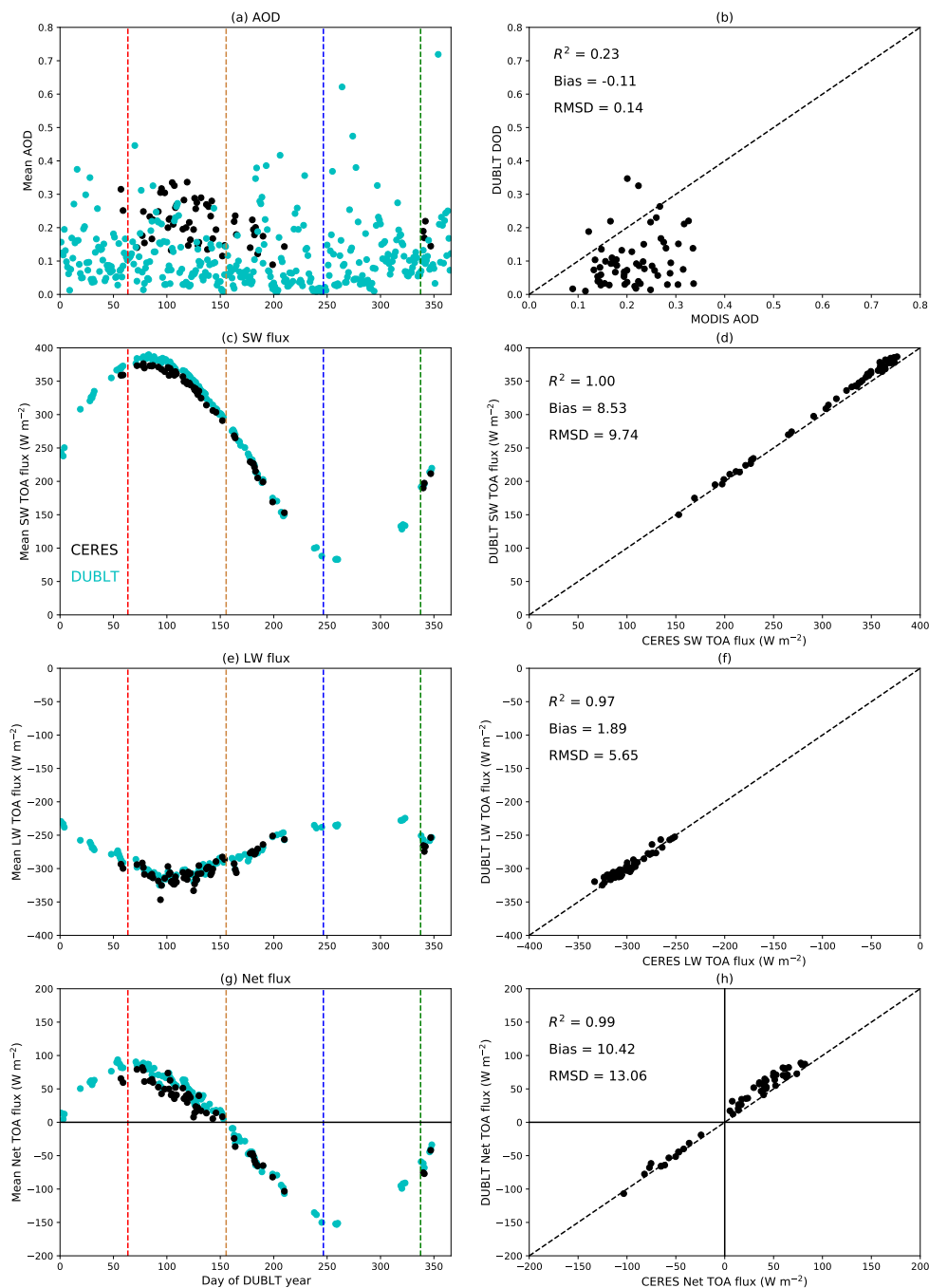
Figure 3. Timeseries plots of daily mean DUBLT DODs and Aqua MODIS AODs, DUBLT and Aqua-CERES SW, LW, and net fluxes, averaged over the Aralkum (see the red box in Fig. 1). For the DODs and DREs only grid cells with a cloud cover < 1% go into the data subset for each daily point in the timeseries. Of the 201 grid cells in the Aralkum, more than 10% of the grid cells must fulfil this criterion in order for the point to go into the timeseries. A total of 53 days go into this co-located data subset. The dashed vertical lines denote the change of the seasons: the red line is the start of summer (1st June), the brown line the start of autumn, the blue line the start of winter, and the green line the start of the second spring (1st March 2016). **8**

and 16th) which had the highest daily emissions. Within the two emission timeseries (panels (a) and (b)) it seems to appear that emission occurs somewhat more frequently in the morning: for cloud-free grid cells (cloud cover $< 1\%$) the yearly total

180   of the 0300-0900 UTC emissions is 1.23 Tg, while for 1500-2100 UTC it is 0.56 Tg. However under all-sky conditions these values show more equivalence at 7.51 and 5.22 Tg, showing that there is a larger fraction of the evening emissions occurring under cloudy skies: 10.8% of the evening emissions occur under clear-skies as opposed to 16.4% in the morning.

Due to the lag in dust accumulation in the atmosphere after emission, and due to external dust sources, this discrepancy between the morning and evening emissions is not replicated in the DODs. The mean values of the points in the cloud-screened

185   timeseries are 0.104 at 0900 UTC and 0.093 at 2100 UTC. As with the emissions, the day with the peak morning DODs is 18th December 2015 (see also Figure 12(c-d) in BHS22 for the DOD case study of this day). This is also the day with the largest Aralkum mean values of SW SFC cooling and LW SFC heating, at -71.1 and +32.8 W m^{-2} respectively in the Present scenario. In the atmosphere the SW and LW DREs almost exactly balance each other out on this day, with a SW DRE of +25.0 W m^{-2} balanced against a LW DRE of -25.7 W m^{-2}, showing how the most prominent dust events do not necessarily

190   lead to the clearest radiative heating or cooling situations. In general, however, the net effect of dust over the Aralkum during the daytime is to cool the surface and warm the atmosphere, DREs which are dominated by the SW effect. Meanwhile at night there is of course no instantaneous SW effect, so the nighttime SFC and ATM DREs are governed solely by the LW radiative heating and cooling, respectively.

Considering the explicit effects of dust on the atmospheric radiation environment, it is instructive and intuitive to consider

195   first an instantaneous case study, before aggregating the simulation output to explore the relationships between variables. As indicated by the dust emissions in Fig. 4, dust activity tends to occur irregularly on an event basis, such that the yearly averages may not always be a clear guide as to the patterns that occur during a substantial dust outbreak. Moreover, by mapping consecutive timeslots it is possible to observe the progression of the radiative effects of an individual dust event with respect to the time-of-day as well as in relation to the DODs and cloud cover. Figure 5 depicts the radiative effects of a notable

200   Aralkum dust event from 17th March 2016, a day which contributed to the strong accumulated dust emissions driven by the westerly winds that were characteristic of the spring months of the simulation year (see Figure 10 in BHS22). This day had a total Aralkum dust emission of 0.86 Tg (the day with the sixth highest emissions during the year), and was the third day of a three-day period from 15-17th March which is preeminent amongst Aralkum dust events during the DUBLT simulation year: this period was responsible for Aralkum dust emissions of 4.99 Tg out of a yearly total of 27.1 Tg, and had the two highest

205   ranked days for Aralkum dust emission during the year. These emissions were, however, co-located with extensive cloud cover except on the third day of the event when the daily average cloud cover over the Aralkum reduced to 69.8%, an opening which permits a look at dust's radiative effects. Four timeslots are mapped in Fig. 5. Dust emissions occurred primarily during the morning hours, driven by westerly winds and transported eastwards over southern Kazakhstan. The earliest and thickest portion of the dust event was co-located with cloud, hindering the radiation simulations, however sufficient dust was still present in the

210   cloud-free areas such that its effects can be discerned.

During 17th March 2016, the maximum surface radiative cooling and atmospheric heating occurred in the early afternoon at 0900 UTC, with a minimum instantaneous SFC DRE of -201 W m^{-2} and a maximum ATM DRE of +68 W m^{-2}, resulting in a
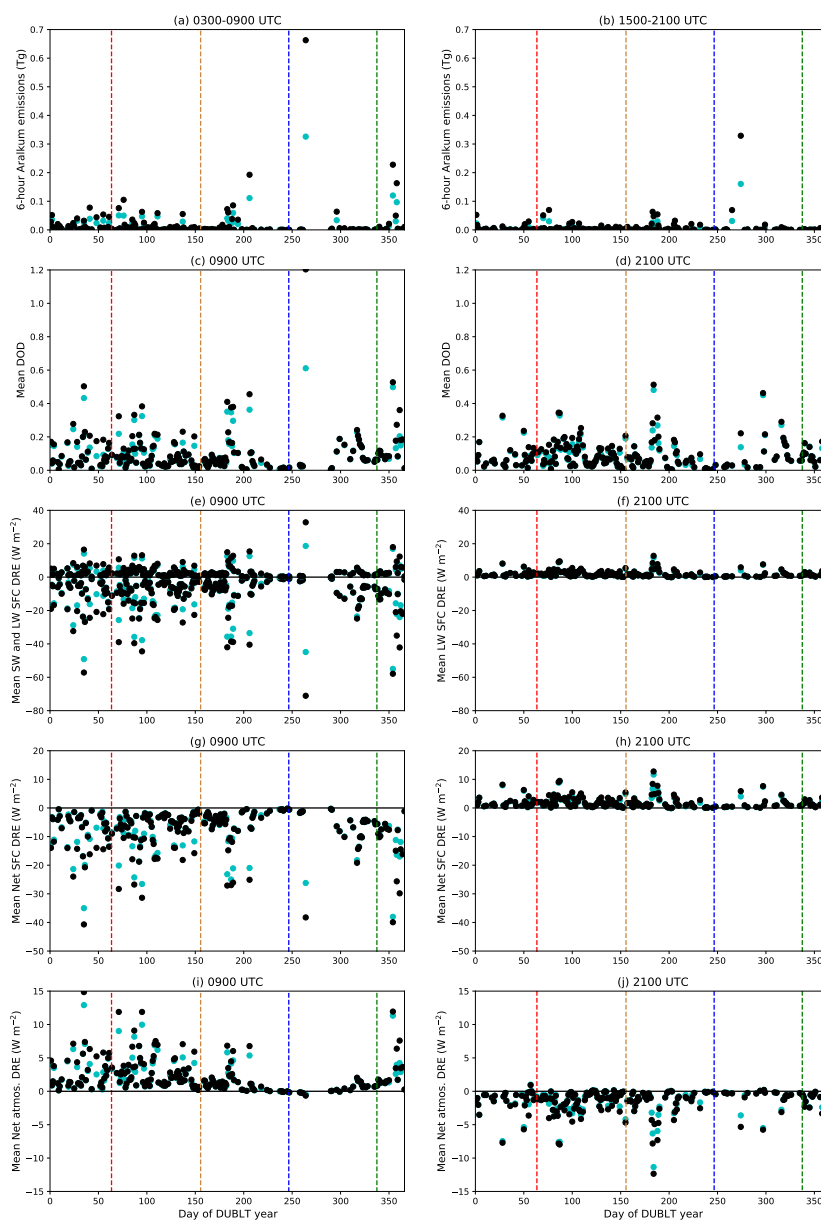
Figure 4. Timeseries plots of 6-hourly accumulated dust emissions, instantaneous DODs and dust DREs averaged over the Aralkum for (left) 0900 UTC, and (right) 2100 UTC. 0900 UTC is ~1300 local time, and 2100 UTC is ~0100 local time. Only grid cells with a cloud cover < 1% go into the data subset for each point in the timeseries. Of the 201 grid cells in the Aralkum, more than 10% of the grid cells must fulfil this criterion in order for the point to go into the timeseries. For the emissions, the values are the totals over the Aralkum box for the preceding 6 hours, i.e. 0300-0900 UTC and 1500-2100 UTC. In panel (e) points with negative values are SW, positive values indicate LW. The black points represent the baseline Present DUBLT scenario and the cyan points represent DUBLT_PAST. The dashed vertical lines denote the change of the seasons: the red line is the start of summer (1st June), the brown line the start of autumn, the blue line the start of winter, and the green line the start of the second spring (1st March 2016).
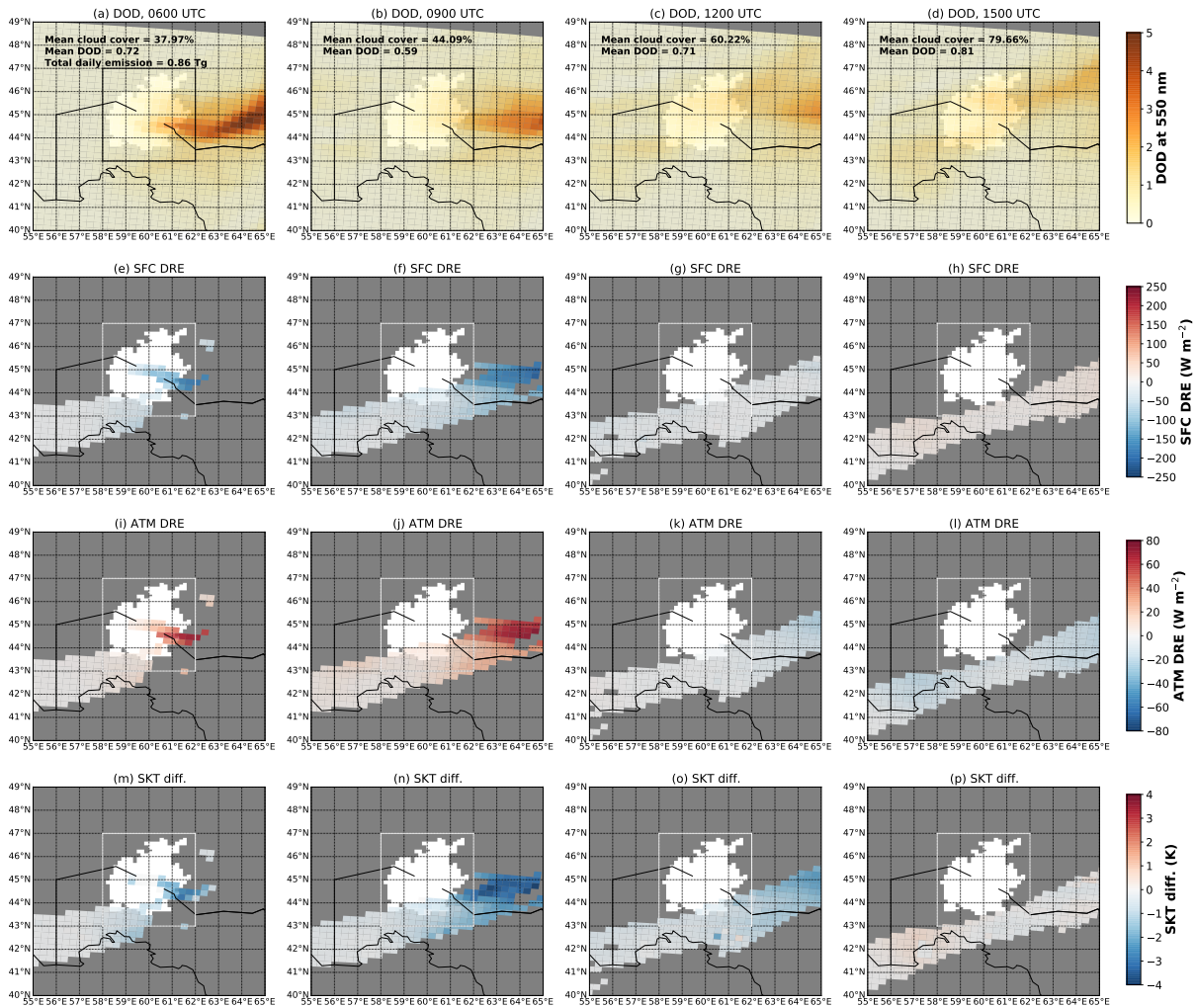
Figure 5. Case study of an Aralkum dust event on 17th March 2016, 3-hourly from 0600 to 1500 UTC left-right, modelled by the DUBLT_PRESENT scenario. The first row shows the instantaneous DODs, the second row the SFC DREs, the third row the atmospheric DREs, and the fourth row the differences in the skin temperature with respect to the non-dust case. Grey grid cells have a cloud cover $\geq 1\%$, and hence are regarded as missing data. The stated values of the mean cloud cover and DOD, and the total daily emission, are for the entire region of the Aralkum within the square box (43-47°N, 58-62°E).

maximum SKT cooling of -3.8 K. Meanwhile from left to right the diurnal cycles in the radiative effects are clearly hinted at, with SFC cooling and ATM heating during the day giving way to SFC heating and ATM cooling later into the afternoon and into the night. The ATM DRE appears to flip sign earlier in the afternoon than does the SFC DRE, indicative of the stronger SW SFC effect during the day, compared to both the LW effect and the daytime SW atmospheric absorption. There is more

215

of a lag in the skin temperature response compared to the radiative fluxes, such that some SKT cooling is still apparent in the early evening (Fig. 5(p)) to the south and east of the Aralkum.

The physics of the general situation over the Aralkum region is described in the maps of aggregated yearly mean SFC and
220 ATM DREs in Fig. 6, subdivided and binned by ranges of the solar zenith angle (SZA). The top row indicates the nighttime situation, while the descending rows refer to lower SZA ranges, i.e. higher solar elevation. It is self-evident that under pristine-sky conditions the surface and the atmosphere are heated when the sun is high during the day and cooled during the night: these are quantified in the labelled fluxes, indicating the consequences of the surface properties for the overall radiative environment, and are considered here for reference. At the surface, the nighttime heating effect of dust appears to transition to the daytime
225 cooling effect at an SZA of $\sim$75° (Fig. 6, panels (c) and (e)), with the most substantial SFC cooling effects due to dust occurring over Turkmenistan's Karakum Desert at lower SZAs (panel (i)). Closely related to this, the Karakum is also where the largest atmospheric heating effects due to dust are simulated (panel (j)), a consequence of relatively frequent dust activity and Turkmenistan's southern location within the region. Meanwhile the nighttime cooling effect of dust in the atmosphere transitions to the daytime heating effect approximately within the 60-75° range (Fig. 6, panel (f)), due also to the transition in
230 the pristine-sky net flux, with an apparent north-south contrast in cooling and heating over the Kyzylkum and the Karakum, respectively.

4 Changes in dust radiative effects due to the expansion of the Aralkum

The extent to which the expansion of the Aralkum has perturbed the regional radiation balance depends on the magnitude of the increase in dust presence and also on the temporal distribution of the additional dust. As reported in BHS22, within the
235 simulations the dust emissions from the Aralkum box increased from 14.3 Tg year^{-1} in the DUBLT_PAST scenario (from the barren land around the Aralkum and that portion of the Aral Sea that had already dried out by the 1980s and 1990s) to 27.1 Tg year^{-1} in the DUBLT_PRESENT scenario, a doubling of the overall emissions. What this means for the monthly mean DODs over Central Asia is depicted in Fig. 7, which also displays the prominence of the Karakum as a dust source during spring and summer, while the Aralkum becomes the more dominant regional source in December and March. The maps
240 of DUBLT_PRESENT - DUBLT_PAST DOD differences are particularly instructive as to the extra dust that would not be in the atmosphere were it not for the desiccation of the Aral Sea, highlighting also November (panel (q)) as a month with extra dust provided by the Aralkum. In contrast, a reduction in dust presence is apparent especially in October (panel (p)) over western Turkmenistan and the Caspian Sea, identifying the Garabogazköl Basin as a dust source during the 1980s prior to its re-inundation (see also BHS22 for further details). For simplicity, with the influence of the Garabogazköl Basin as a relevant
245 caveat, the DUBLT_PRESENT - DUBLT_PAST difference will henceforth be referred to as the 'DUBLT_ARALKUM' scenario, given that Aralkum dust is not added to a pristine dust-free regional environment, but to a region including pre-existing dust-producing deserts.

The radiative effects of extra dust in the atmosphere are dependent on the solar elevation, as previously indicated by Fig. 6. The patterns of the DREs over the Aralkum with respect to the associated SZAs and DODs are described in more detail by
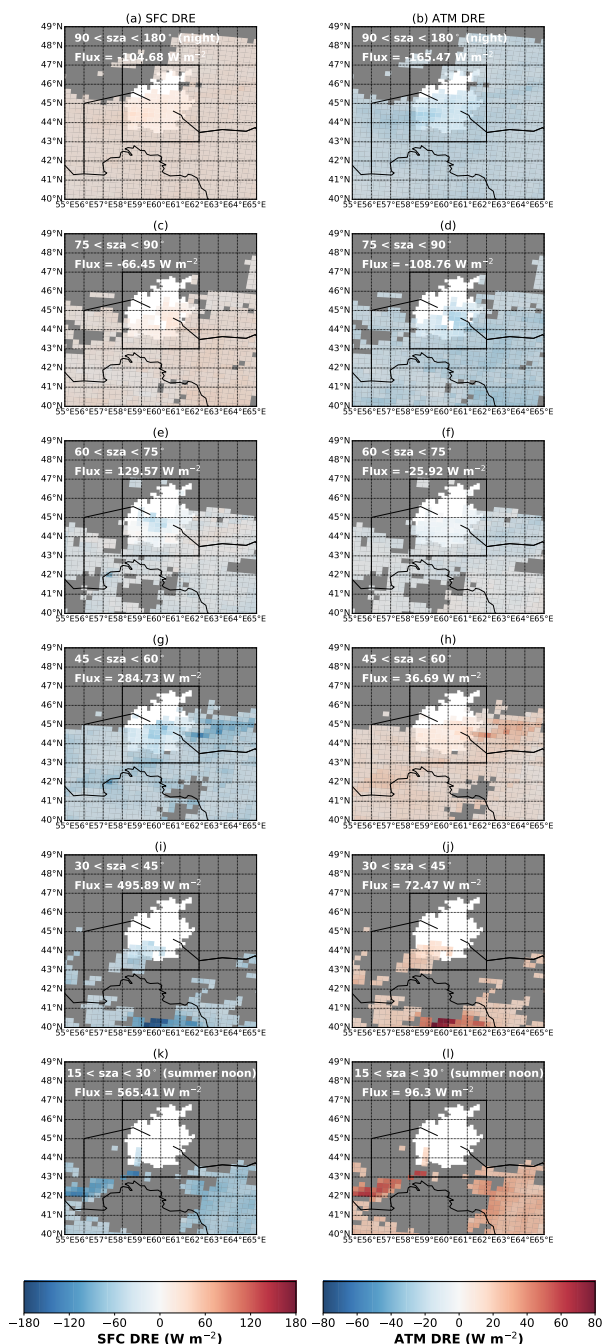
Figure 6. Maps of Present dust SFC (left column) and ATM (right column) DREs for DODs > 0.5, cloud-screened in both the DUBLT_PRESENT and DUBLT_NODUST scenarios to a maximum cloud cover of 1%, from the entire DUBLT simulation year. Each row is for a specified SZA range, as indicated (one nighttime bin in the top row, 15° SZA bins during the day). The marked fluxes are the pristine-sky mean net fluxes in the DUBLT_NODUST scenario, i.e. excluding dust and cloud.
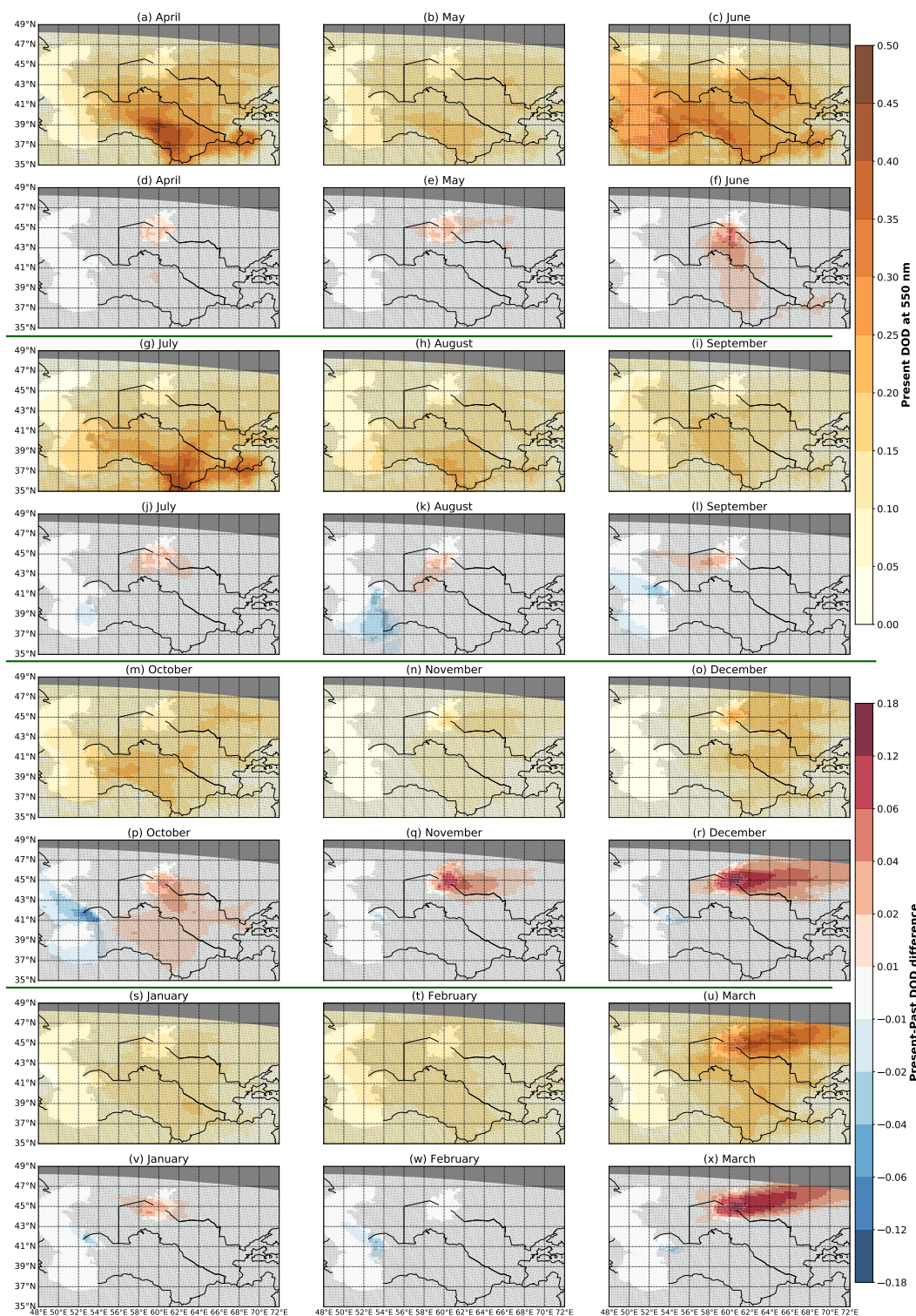
Figure 7. Maps of monthly mean DUBLT_PRESENT DODs over Central Asia, along with the associated mean DUBLT_PRESENT - DUBLT_PAST DOD differences (DUBLT_ARALKUM).
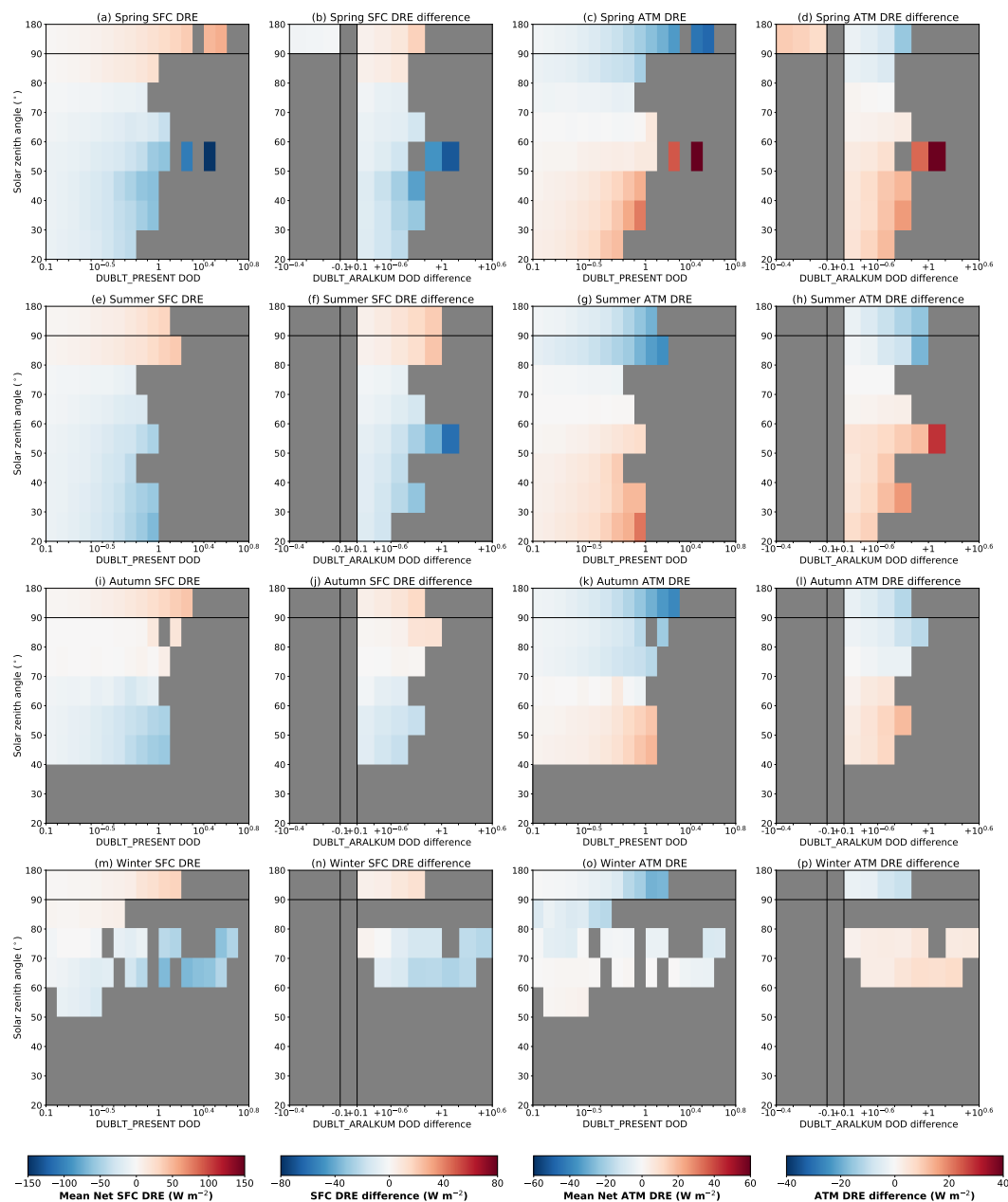
Figure 8. Seasonal mean DUBLT_PRESENT and DUBLT_PRESENT - DUBLT_PAST (DUBLT_ARALKUM) net SFC (left columns) and ATM (right columns) DREs, binned as functions of DUBLT_PRESENT DODs (first and third columns) and DUBLT_Aralkum DOD differences (second and fourth columns), and of SZA for each grid cell and timeslot within the Aralkum. The Aralkum is here bound by the longitudes 58-62°E and by the latitudes 43-47°N, see also the box in Fig. 1 and subsequent maps. The seasons are MAM, JJA, SON, and DJF. The SZA bin width is 10° during the day, with one bin at night: the solid black horizontal line denotes the day-night boundary. Meanwhile the DOD bin widths are logarithmic, and each column has its own colour scale. The allowable cloud threshold is 1% in all three simulations.

Fig. 8, in relation also to the associated DOD differences between the Present and Past scenarios. Depicted here are both the DUBLT_PRESENT DREs (for context as to the total values) and the DUBLT_ARALKUM DRE differences to highlight the impact of the additional Aralkum dust. It is to be expected that the largest absolute values of the DREs will be at higher DODs, and during the daytime at lower SZAs, due to the stronger SW effect of the dust compared to its LW effect. Summarising the contrasting SW and LW effects, in the SW there is no effect at night while during the day at higher DODs dust causes SW SFC cooling and ATM heating, while in the LW there is much less dependence on the time-of-day with dust causing LW ATM cooling and SFC heating. The dominance of the SW effect during the daytime is apparent, see the situation in spring (panels (a-d)) at high DODs in the SZA bin between 50 and 60°: it is during the spring that the maximum bin SFC cooling and ATM heating occurs, with daytime SFC cooling in the Present scenario of -147.5 W m^{-2} and ATM heating of +59.6 W m^{-2} in the 50-60° SZA bin, primarily due to the March 2016 dust events. The equivalent high positive DOD difference bin in the DUBLT_ARALKUM case gives an extra SFC cooling due to Aralkum dust of -67.7 W m^{-2}, and an extra ATM heating of +39.1 W m^{-2}. Given the doubling of the Aralkum's emissions from Past to Present, the ratios of these DRE maxima imply that the ATM DREs are slightly more responsive to the presence of Aralkum dust compared to the SFC DREs.

There are daytime bins with higher DODs in winter (during this season the daytime SZAs are higher over the Aralkum) than in the spring, especially when considering the Present with respect to the Past, however these high DOD bins are in the transition region of the SZA range in which there is more ambiguity as to whether the atmospheric SW heating or LW cooling effect would dominate, and where both the surface and atmosphere may cool in the same bins. In the Present scenario the greatest SFC cooling in winter is -67.8 W m^{-2}, but at a DOD of just 1.6-2.0 in the 60-70° SZA bin, while the greatest ATM heating is just +2.4 W m^{-2} within the DOD bin from 0.25-0.32 ($10^{-0.6}$-$10^{-0.5}$) and an SZA from 50-60°. The highest daytime DOD bins (> 2.0) in winter have DREs which are cooling both at the surface and in the atmosphere. More dust does not automatically imply a greater radiative effect.

At night, the Present DREs have opposite signs compared to during the day, due to the controlling LW effect, i.e. SFC warming and ATM cooling. For the nighttime spring is again the season with the highest Present DODs and DREs, although it appears also to be the season with the relatively uncommon occurrence of higher Past DODs compared to the Present (due to other formerly dry lakebeds such as the Garabogazköl Basin). In the Present scenario the maximum bin SFC nighttime warming is +53.9 W m^{-2} (compared to minimum SFC daytime cooling of -147.5 W m^{-2}), while the minimum ATM cooling is -47.2 W m^{-2} (compared to maximum daytime ATM warming of +59.6 W m^{-2}). This quantifies the relatively weak LW effect at night compared to the stronger and competing SW and LW effects during the day. Meanwhile the additional Aralkum dust (Present-Past) adds up to an extra +20.5 W m^{-2} of SFC heating in the summer, and an extra -15.7 W m^{-2} of ATM cooling also in summer. The additional effects of Aralkum dust appear to be less significant at night than during the daytime.

Analysing this information from a different perspective so as to investigate further the significance of the impacts of Aralkum dust on the overall radiation budget, Fig. 9 seeks to elucidate the changes in the distributions of the radiative effects between the Past and Present by considering their distributions on the monthly timescale, along with the distributions of the DODs and the Present DREs weighted by the DOD (the 'DRE efficiency'). By considering the DRE efficiencies it is thereby possible to extract the seasonal cycle of the DODs from that of the DREs. The plots are subdivided into nighttime and daytime data
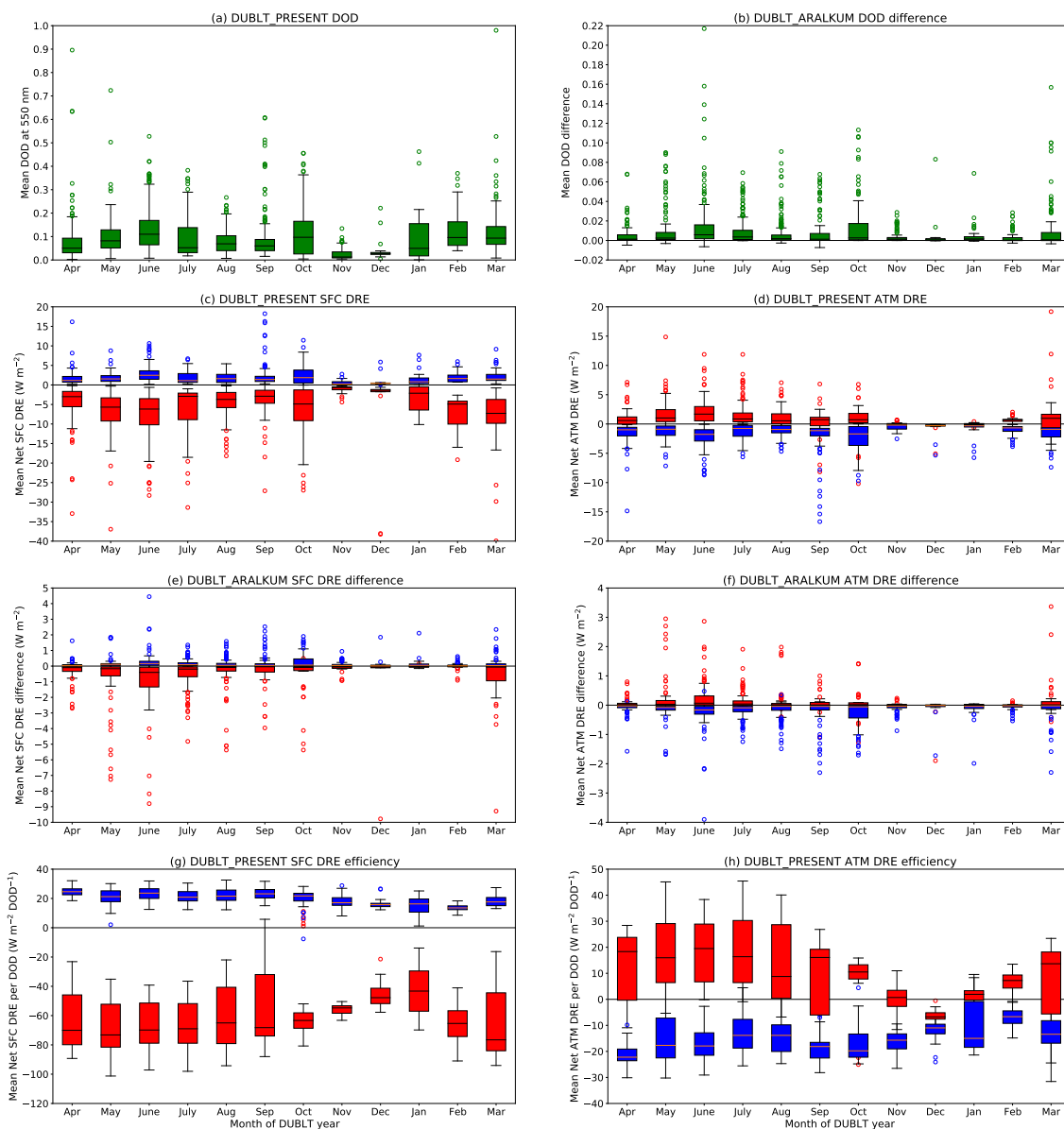
Figure 9. Boxplots displaying (top row) the monthly DOD values averaged over the cloud-free grid cells of the Aralkum (per grid cell the maximum allowable cloud threshold is 1% in both the dust and the NODUST scenario, with > 10% of grid cells required to be cloud-free for a timeslot to be included in the monthly statistics), in the Present scenario, and their Present-Past (DUBLT_ARALKUM) differences, with outliers included for points beyond the quartile ranges. In the second and third rows are the associated monthly net (left column) SFC and (right column) ATM DRE values. In the bottom row are the corresponding ranges for the DREs weighted by the DODs. For the DREs the timeslots are subdivided by time-of-day: the blue bars and outliers (marked by circles) denote the nighttime timeslots, with an SZA $\geq 90°$, while the red bars and outliers denote the daytime timeslots, here defined as having an SZA $< 75°$. Therefore daytime timeslots at low solar elevation are excluded. The y-axes are truncated for clarity, but there are outliers. In panel (a) there are outliers in December at DODs of 1.20 and 1.78, while in panel (b) there are outliers in December at +0.59 and +0.92, and in March at +0.42. In panel (c) there are outliers in April at +23.8 W m^{-2} (night), in May at -40.7 W m^{-2} (day), and in March at -61.8 W m^{-2} (day). In panel (d) there is a nighttime outlier in April at -21.1 W m^{-2}. In panel (e) there are daytime outliers in December at -12.0 W m^{-2} and in March at -12.9 and -23.0 W m^{-2}. In panel (f) there is a daytime outlier in March at +8.9 W m^{-2}.

subsets, emphasising the distinctions between the cooling and warming modes and the primacy of either the SW or LW effects, recalling from Figures 6 and 8 that the net dust radiative effects are negligible when the sun is low above the horizon. June and October appear here to be particularly dusty months in general over the Aralkum in the Present scenario (panel (a)), due to Aralkum dust (b), but December and March are the months with the biggest individual events. In most months dust cools the surface during the day and warms it at night, and warms the atmosphere during the day and cools it at night; Aralkum dust (denoted by the Present-Past differences) typically acts to enhance these patterns. In general, the strongest persistent Present and Present-Past DREs occur during the summer and spring months when there is the most solar and thermal radiation available for dust to interact with, a point which is emphasised by the DRE efficiencies in panels (g) and (h). At the surface dust is more efficient in its SW cooling effect than it is in its LW heating effect. It is also clear that there is a stronger seasonal cycle in the DRE efficiencies during the daytime compared to during the night, as a consequence of the seasonal variations in the solar zenith angle.

Table 1. Accompanying Fig. 9, the yearly mean Aralkum area-averaged and cloud-screened values of the DODs and the SFC and ATM DREs (DUBLT_PRESENT and DUBLT_ARALKUM), along with their associated standard deviations. 'Day' is at an SZA $< 75°$ and night is at an SZA $\geq 90°$. DREs have units $\mathrm{W\,m^{-2}}$.

	All	Day	Night
(a) DUBLT_PRESENT DOD	0.099±0.107	0.103±0.126	0.094±0.091
(b) DUBLT_PAST DOD	0.089±0.085	0.090±0.090	0.087±0.084
(c) DUBLT_ARALKUM DOD	0.0097±0.0339	0.0130±0.0489	0.0068±0.0134
(d) DUBLT_PRESENT SFC DRE	-1.34±6.19	-6.09±6.64	+2.03±2.33
(e) DUBLT_ARALKUM SFC DRE	-0.15±1.19	-0.64±1.64	+0.20±0.42
(f) DUBLT_PRESENT ATM DRE	-0.62±2.91	+1.24±2.25	-1.55±2.12
(g) DUBLT_ARALKUM ATM DRE	-0.05±0.51	+0.15±0.54	-0.19±0.38

Diverting briefly to consider the totality of this particular year, Tables 1 and 2 show that at the surface the daytime radiative cooling effect dominates, while in the atmosphere the nighttime cooling effect is also dominant, with Aralkum dust enhancing both of these effects. There are slightly higher DODs during the day than during the night in the Present scenario (Table 1(a)), while dust from the Aralkum (c) is added particularly prominently to the (cloud-free) atmosphere over the Aralkum during the daytime compared to during the night: in the Past scenario (b) there were much more balanced average dust loadings between day and night. This relates also to the apparent behaviour of evening dust emissions occurring more frequently under cloudy skies which was previously noted in relation to Fig. 4, dust loadings which would be more frequently cloud-screened for the purposes of analysing the dust DREs. In the Present scenario daytime cooling at the surface (d) is comparatively stronger than daytime heating in the atmosphere (f), while the nighttime SFC and ATM effects are broadly equivalent with each other. Aralkum dust adds an extra -0.15±1.19 $\mathrm{W\,m^{-2}}$ of cooling at the surface (e), up to -23.0 $\mathrm{W\,m^{-2}}$ on an event basis, and an extra -0.05±0.51 $\mathrm{W\,m^{-2}}$ of cooling in the atmosphere (g), with extrema of -5.82 and +8.91 $\mathrm{W\,m^{-2}}$.

Table 2. Accompanying Table 1, the minimum and maximum Aralkum area-averaged and cloud-screened values of the DODs and the SFC and ATM DREs (DUBLT_PRESENT and DUBLT_ARALKUM). DREs have units $\mathrm{W\,m^{-2}}$.

	Minimum	Maximum
(a) DUBLT_PRESENT DOD	0.00	1.78
(b) DUBLT_PAST DOD	0.00	0.86
(c) DUBLT_ARALKUM DOD	-0.01	+0.92
(d) DUBLT_PRESENT SFC DRE	-61.8	+23.8
(e) DUBLT_ARALKUM SFC DRE	-23.0	+5.98
(f) DUBLT_PRESENT ATM DRE	-21.1	+19.2
(g) DUBLT_ARALKUM ATM DRE	-5.82	+8.91

Returning to the seasonal cycle, it is again clear that in the Present scenario the daytime SFC cooling effect (Fig. 9(c)) is more significant than both the nighttime SFC heating effect and the ATM (panel (d)) cooling and heating effects. Similarly the Aralkum's dust contributes most to enhanced SFC daytime cooling (e), especially in June and March, while the Aralkum's daytime and nighttime atmospheric effects (f) are fairly well balanced. During winter the DUBLT_PRESENT and DUBLT_ARALKUM DREs are comparatively weak, especially in November and December when only very occasional dust outbreaks perturb the regional radiation environment. December in particular is an unusual month for the Aralkum, as being the one month in the year when dust typically cools the atmosphere both during the night and during the day (although there are also daytime cooling outliers in other months especially in September, October, and March). Correspondingly, in December during the day dust acts to cool both the surface and the atmosphere. The unusual nature of the December effect is particularly prominent in the DRE efficiencies (h).

5 Perturbations to the atmosphere due to the presence of Aralkum dust

Given these quantified simulated dust DREs, and the differences between the Past and the Present epochs, what are the implications for the atmospheric state in response to the presence of Aralkum dust aerosol? COSMO-MUSCAT simulates radiative feedback of the dust on the atmospheric state, and so it is therefore possible to make quantitative estimates of the differences in the atmospheric variables between the various scenarios. Figure 10 maps the differences in the skin temperature (SKT), the air temperature at 950 hPa (T950hPa, i.e. ∼500 m above sea level), the pressure at mean sea level (PMSL), and the total cloud cover between the Present and the Past scenarios, so as to isolate the effect on the atmosphere of the additional Aralkum dust. It is important to consider these changes primarily on longer timescales given the cumulative perturbations by Aralkum dust to the Central Asian atmosphere, and the associated lag times in the response of the atmosphere to additional dust aerosol. Given the noise in the data, in order to identify signals in the atmospheric variables more clearly Gaussian smoothing has been applied to the data (e.g. Miinalainen et al., 2021, see supporting information), with a σ value of 2. These plots should also be
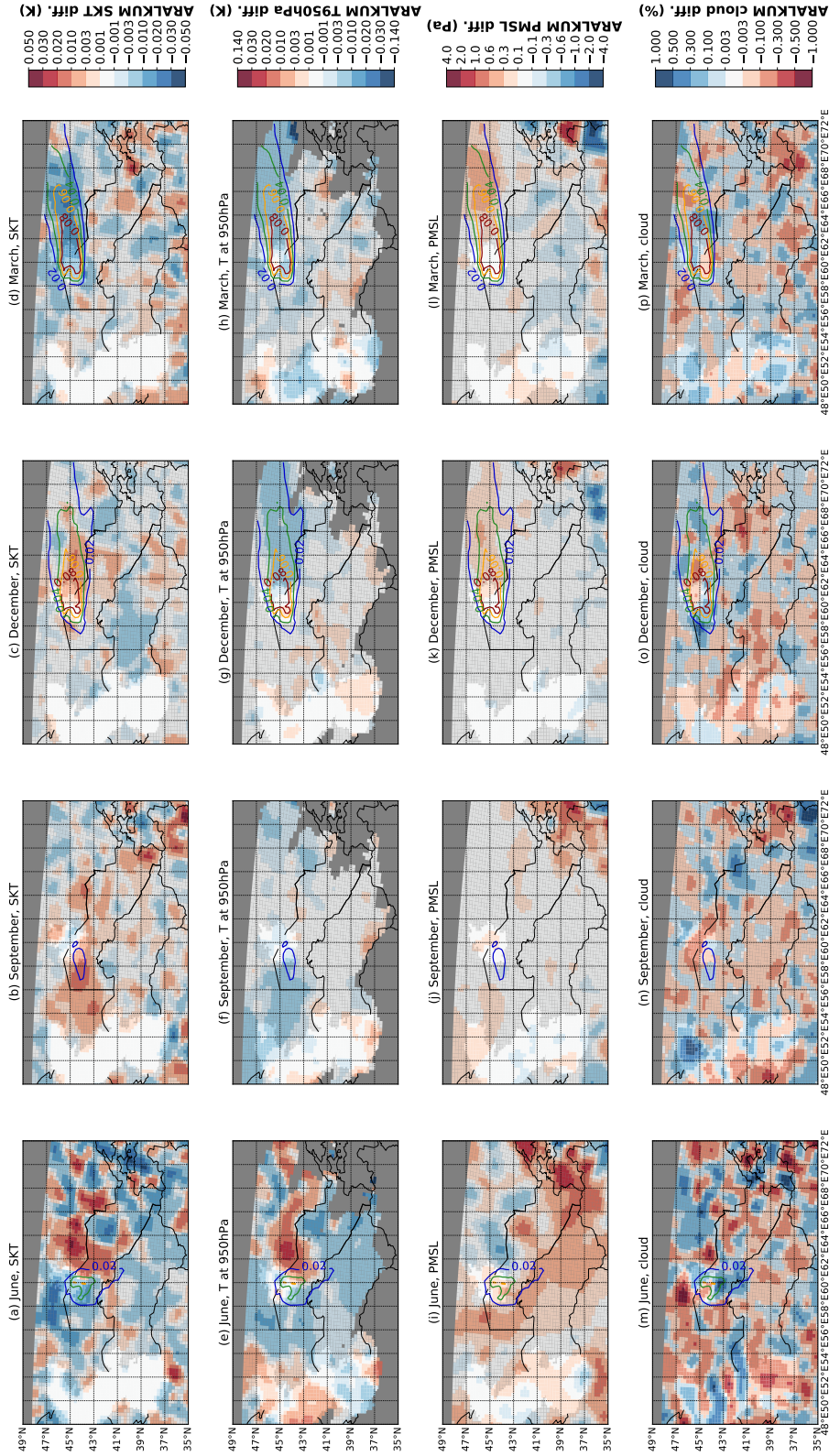
Figure 10. Maps of smoothed perturbations (DUBLT_PRESENT - DUBLT_PAST, i.e. DUBLT_ARALKUM - DUBLT_PAST, and total cloud cover (bottom row), for June, September, December, and March. Contour lines indicate the corresponding monthly mean DUBLT_ARALKUM DOD values, so as to isolate the spatial distribution of additional Aralkum dust. Gaussian smoothing has been applied to the data ($\sigma = 2$), note also that the colour scales are non-linear.

considered with reference to the DUBLT_PRESENT DODs and DUBLT_ARALKUM DOD differences mapped in Fig. 7; it is also important to recognise that these mapped perturbations are monthly averages, and so the magnitude of the perturbations
330 may appear modest. Furthermore, it is relevant to note that the perturbations are often larger over the mountain regions to the south-east (in Tajikistan, Afghanistan and Kyrgyzstan) where the orography can introduce supplementary effects: these effects will not be considered in this discussion.

The atmospheric perturbations differ according to the atmospheric dust distribution and the season of the year, and are highly non-linear in their responses, with effects propagating to areas remote from the Aralkum. Dust directions from the Aralkum
335 for this simulation year are typically southwards in June (a direction previously noted by other authors including Wang et al. (2022)), westwards in September, and eastwards in December and March. Bearing that in mind, the SKT response to the prevailing dust directions appears to be warming in June, September and December (up to +0.020 K), but cooling in March, down to -0.021 K. Meanwhile the T950hPa response is ambiguous in the hotter month of June, but notably cooling in the cooler months of September, December and March, down to -0.009 K. More consistent patterns seem to be apparent in the PMSL
340 response, typically with increases in the pressure downwind of the Aralkum of up to +0.49 Pa in June, December and March, with the increased pressure pattern being particularly prominent in March. The PMSL response in September is comparatively negligible. The June PMSL pattern (Fig. 10(i)) shows a degree of complexity, despite the increased pressure downwind of the Aralkum, with perturbations nearby to the east of the Aralkum: positive peaks lie immediately to the west and to the east in northern Uzbekistan (up to +0.76 Pa), but balanced by a negative trough to the east in southern Kazakhstan (down to -0.64 Pa).
345 Given the prevailing meteorology of the region depicted in Fig. 1, this would therefore imply a strengthening of the Siberian High in the winter and early spring (of the simulation year), and a weakening of the Central Asian Heat Low in summer. Both weather patterns mainly influence the locally prevailing weather conditions and air mass transport and, therefore, also the occurrence of dust storms in Central Asia, but also play an important role in the global atmospheric circulation context. The heat low ventilates the heated summertime land masses of Central Asia by attracting cooler and moist air from the Central
350 Indian Ocean. The Siberian High is the largest high-pressure system that prevails in the northern hemisphere during the winter. An intensification leads to increased pressure gradients and thus to stronger dust-producing surface winds over the Central Asian desert regions.

Pressure and temperature perturbations to the atmospheric environment would also influence cloud formation and lifetime, hence it is also clear that Aralkum dust may have semi-direct effects on the atmosphere (e.g. Meier et al., 2012). While the
355 effects on the clouds are predominantly stochastically distributed in nature, a direct correlation with the dust immediately above the Aralkum can be seen, particularly in June, with a decrease in cloud cover (Fig. 10(m)) in the vicinity of the Aralkum by as much as -0.72%. It can also be seen that the changed cloud cover has a similar magnitude of effect on the surface temperature as the direct radiative influence of the dust. In particular, regions with a significant increase in cloud cover (June and March) are clearly recognisable by a decrease in temperature. Finally, there are also displacements in the precipitation spatial distribution
360 (not shown), with negative perturbations downwind of the Aralkum up to -1.5 mm month^{-1} and positive perturbations up to +1.1 mm month^{-1}.

6   Conclusions

Building on the findings of BHS22, which described the impact of the desiccation of the Aral Sea in Central Asia on the quantity and distribution patterns of dust emitted from the Aralkum, this current paper investigates the impact of this increase in dust
365   activity on the radiation environment in the vicinity of the Aralkum. Referring back to the questions posed at the end of Section 1, what are the consequences of the expanded Aralkum for the radiative effects of dust in the region? Given that dust activity primarily occurs in the form of discrete dust events, it is clear that on the yearly timescale the perturbation of the surface and atmospheric radiation environment due to dust may be modest (in the baseline Present scenario the yearly average cloud-screened net SFC dust DRE over the Aralkum is -1.34±6.19 W m^{-2}, while the average net ATM DRE is -0.62±2.91 W m^{-2}). However
370   during individual dust events the DREs can be markedly more significant, with grid cells experiencing up to -207 W m^{-2} of instantaneous net SFC radiative cooling and +95 W m^{-2} of net atmospheric radiative heating due to dust, of which -116 W m^{-2} of surface cooling and +54 W m^{-2} of atmospheric heating are due to Aralkum dust.

What are the patterns of the radiative cooling and warming effects of dust on the surface and atmospheric environment of the Aralkum region? As with other desert regions, the intensity and the sign of the dust DRE over the Aralkum is highly
375   dependent on the time of day and the season during the year in which the dust events occur, primarily as a function of the solar insolation (considered here with reference to the SZA). At the surface, dust tends to cause radiative cooling during the daytime and heating during the night, transitioning between the two regimes in an SZA range of ∼70-80°: dust events occurring during these transition periods of the day will have a negligible impact on the surface radiation environment, while the strongest impacts occur at local noon. It is also apparent that dust events lasting between the day and the night (e.g. Fig. 5) will cause
380   opposite radiative impacts at different times during its life-cycle. Meanwhile in the atmosphere dust tends to cause radiative heating during the day and radiative cooling at night, transitioning in the SZA range between ∼60-70°. The radiative effects typically have stronger intensities during daylight (i.e. heating in the atmosphere), however since the transition point is <70° the larger fraction of the diurnal cycle is contained within the 'night-time' mode, and hence atmospheric cooling is more frequent to the extent that the overall effect on the atmosphere on the yearly timescale is also cooling (as at the surface).

385   How have the patterns of the dust DREs changed as the Aralkum has expanded? Considering the changes between Past and Present epochs, the near-doubling in dust emissions over the Aral Sea / Aralkum region due to the expansion of the barren lakebed has resulted in increases in the occurrence of both radiative cooling and radiative warming events at the surface and in the atmosphere. These 'new' dust events, that would not have occurred without the desiccation of the Aral Sea, do not occur year-round: instead they occur as episodes during June, September, November, December (weak atmospheric radiative cool-
390   ing), and March (occasionally strong atmospheric warming). Compared to the Past scenario ('pre-desiccation'), Aralkum dust is added to the cloud-free atmosphere more heavily during daytime than during nighttime, leading typically to an enhanced cooling effect at the surface (-0.15±1.19 W m^{-2}), clearly outweighing the enhanced heating at night. However in the atmosphere, since the daytime heating effect is weaker than the nighttime cooling effect, additional Aralkum dust also tends to cool the atmosphere on the yearly timescale, by -0.05±0.51 W m^{-2}, although instantaneously there are greater atmospheric heating
395   than cooling events (up to +8.91 W m^{-2} compared to -5.82 W m^{-2}).

As to whether these radiative effects of Aralkum dust have had consequences for the wider atmospheric environment, these appear to be modest but potentially of some significance. Through the radiative feedbacks contained within the regional modelling approach it is possible to make quantitative estimates of the perturbations to the atmospheric state due to the addition of Aralkum dust. On the monthly timescale Aralkum dust typically triggers a positive perturbation to the surface pressure (PMSL) by up to +0.76 Pa in the vicinity of the Aralkum, implying a strengthening of the Siberian High in the colder months and a weakening of the Central Asian Heat Low in summer. The consequent effects on the surface and lower atmospheric temperatures are complex (cooling and heating) and may also be connected to semi-direct effects in relation to the perturbations in cloud cover, which vary by as much as -0.72% on the monthly average. The least ambiguous temperature effects occurred in March 2016, the month which saw the biggest dust events of the simulation year, with temperature responses to Aralkum dust which are cooling both on the ground and in the troposphere at 950 hPa, with monthly mean decreases of up to -0.021 K at the surface and -0.009 K in the troposphere.

There remain open questions as to the mineralogy and therefore the optical properties of Aralkum dust, which have not been considered in this paper. It is understood that lakebed dust has a different mineralogy (e.g. Hamzehpour et al., 2022, and others) to dust from older deserts such as the Karakum, presumably with more strongly scattering optical properties due to the enhanced salt content of the dust (e.g. Argaman et al., 2006; Löw et al., 2013; Indoitu et al., 2015, and others), and so it would in future be worthwhile to explore the sensitivity of the radiative impacts of the Aralkum dust to the assumed optical properties of this dust. We therefore recommend further investigation of the spectrally-resolved SW and LW optical properties of Aralkum dust, so as to more robustly simulate the radiative effects of Aralkum dust.

Code and data availability. The COSMO model is distributed to research institutions free of charge under an institutional licence issued by the Consortium COSMO and administered by DWD (see http://www.cosmo-model.org/content/consortium/licencing.htm, last access: 10 October 2023). The COSMO licence also includes access to lateral boundary data provided by DWD. ICON analysis data used for the initial and lateral boundary conditions for the COSMO-MUSCAT model experiments in this study can be downloaded from the DWD PAMORE (Parallel Model data Retrieve from Oracle databases) web-interface (https://www.dwd.de/DE/leistungen/pamore/pamore.html, last access: 10 October 2023). The aerosol-chemistry-transport model MUSCAT is based at least in part on the source code of the COSMO model, and hence redistribution is limited by the COSMO license. The python scripts used to analyse the data and to plot the figures are publicly available on Zenodo (Banks et al., 2023b). The associated COSMO-MUSCAT simulation output data (dust radiative effects, emissions, DODs, and associated atmospheric variables) are also publicly available on Zenodo (Banks et al., 2023a), for the three dust scenarios analysed in this paper: DUBLT_PRESENT, DUBLT_PAST, and DUBLT_NODUST. The Global Surface Water dataset (Global Surface Water, 2016), which is used to distinguish the Past and Present DUBLT scenarios, is provided by the European Commission's Joint Research Centre, part of the Copernicus Programme. CERES radiative fluxes data are provided by NASA's Langley Research Center (CERES Science Team, Hampton, VA, USA, 2023).

Author contributions. JRB performed the COSMO-MUSCAT simulations and the analysis, and designed and wrote the manuscript. BH and KS contributed to the concept and design of the manuscript.

Competing interests. The authors declare that they have no conflict of interest.

430 *Acknowledgements.* JRB has been funded for this work by the Deutsche Forschungsgemeinschaft (DFG), under the project DESERT-TIME (grant number BA 6612/1-1, project number 414044717). Deutscher Wetterdienst (DWD) has provided access to the COSMO model as well as boundary data. CERES data were obtained from the NASA Langley Research Center CERES ordering tool at https://ceres.larc.nasa.gov/data/.

References

435 Alamirew, N. K., Todd, M. C., Ryder, C. L., Marsham, J. H., and Wang, Y.: The early summertime Saharan heat low: sensitivity of the radiation budget and atmospheric heating to water vapour and dust aerosol, Atmospheric Chemistry and Physics, 18, 1241–1262, https://doi.org/10.5194/acp-18-1241-2018, 2018.

Argaman, E., Singer, A., and Tsoar, H.: Erodibility of some crust forming soils/sediments from the Southern Aral Sea Basin as determined in a wind tunnel, Earth Surface Processes and Landforms, 31, 47–63, https://doi.org/10.1002/esp.1230, 2006.

440 Banks, J. R., Brindley, H. E., Hobby, M., and Marsham, J. H.: The daytime cycle in dust aerosol direct radiative effects observed in the central Sahara during the Fennec campaign in June 2011, Journal of Geophysical Research: Atmospheres, 119, 13,861–13,876, https://doi.org/10.1002/2014JD022077, 2014.

Banks, J. R., Heinold, B., and Schepanski, K.: Impacts of the desiccation of the Aral Sea on the Central Asian dust life-cycle, Journal of Geophysical Research: Atmospheres, 127, https://doi.org/10.1029/2022JD036618, 2022.

445 Banks, J. R., Heinold, B., and Schepanski, K.: Dataset associated with Banks et al. (2023): "Radiative cooling and atmospheric perturbation effects of dust aerosol from the Aralkum Desert in Central Asia" [Dataset], https://doi.org/10.5281/zenodo.10143872, 2023a.

Banks, J. R., Heinold, B., and Schepanski, K.: Python code associated with Banks et al. (2023): "Radiative cooling and atmospheric perturbation effects of dust aerosol from the Aralkum Desert in Central Asia" [Software], https://doi.org/10.5281/zenodo.10160848, 2023b.

Breckle, S.-W. and Wucherer, W.: The Aralkum, a Man-Made Desert on the Desiccated Floor of the Aral Sea (Central Asia): General
450 Introduction and Aims of the Book, in: Aralkum - a Man-Made Desert: The Desiccated Floor of the Aral Sea (Central Asia), edited by Breckle, S.-W., Wucherer, W., Dimeyeva, L. A., and Ogar, N. P., chap. 1, pp. 1–9, Springer, 2012.

Brindley, H. E. and Russell, J. E.: An assessment of Saharan dust loading and the corresponding cloud-free longwave direct radiative effect from geostationary satellite observations, Journal of Geophysical Research, 114, https://doi.org/10.1029/2008JD011635, 2009.

CERES Science Team, Hampton, VA, USA: CERES Time-Interpolated TOA Fluxes, Clouds and Aerosols Daily Aqua Edition4A [Dataset],
455 https://doi.org/doi.org/10.5067/Aqua/CERES/SSF1degDay_L3.004A, 2023.

Didan, K.: MYD13C2 MODIS/Aqua Vegetation Indices Monthly L3 Global 0.05Deg CMG V006 [CMG 0.05 Deg Monthly NDVI], accessed: 2018-12-12 from https://doi.org/10.5067/MODIS/MYD13C2.006, 2015.

Doelling, D. R., Loeb, N. G., Keyes, D. F., Nordeen, M. L., Morstad, D., Nguyen, C., Wielicki, B. A., Young, D. F., and Sun, M.: Geostationary Enhanced Temporal Interpolation for CERES Flux Products, Journal of Atmospheric and Oceanic Technology, 30, 1072–1090,
460 https://doi.org/10.1175/JTECH-D-12-00136.1, 2013.

Dubovik, O., Holben, B., Eck, T. F., Smirnov, A., Kaufman, Y. J., King, M. D., Tanré, D., and Slutsker, I.: Variability of Absorption and Optical Properties of Key Aerosol Types Observed in Worldwide Locations, Journal of the Atmospheric Sciences, 59, 590–608, https://doi.org/10.1175/1520-0469(2002)059<0590:VOAAOP>2.0.CO;2, 2002.

Global Facility for Disaster Risk Reduction and Recovery: Weather, Climate and Water in Central Asia: A Guide to Hydrometeorological Ser-
465 vices in the Region, https://www.gfdrr.org/en/weather-climate-and-water-central-asia-guide-hydrometeorological-services-region, 2019.

Global Surface Water: Global Surface Water [Dataset], https://global-surface-water.appspot.com/download, 2016.

Groll, M., Opp, C., and Aslanov, I.: Spatial and temporal distribution of the dust deposition in Central Asia - results from a long term monitoring program, Aeolian Research, 9, 49–62, https://doi.org/10.1016/j.aeolia.2012.08.002, 2013.

Hall, D. K. and Riggs, G. A.: MODIS/Aqua Snow Cover 8-Day L3 Global 0.05Deg CMG, Version 6 [Eight Day CMG Snow Cover],
470 accessed: 2020-04-28 from https://doi.org/10.5067/MODIS/MYD10C2.006, 2016.

Hamzehpour, N., Marcolli, C., Pashai, S., Klumpp, K., and Peter, T.: Measurement report: The Urmia playa as a source of airborne dust and ice-nucleating particles - Part 1: Correlation between soils and airborne samples, Atmospheric Chemistry and Physics, 22, 14 905–14 930, https://doi.org/10.5194/acp-22-14905-2022, 2022.

Haywood, J. M., Francis, P., Osborne, S., Glew, M., Loeb, N., Highwood, E., Tanré, D., Myhre, G., Formenti, P., and Hirst, E.: Radiative
475   properties and direct radiative effect of Saharan dust measured by the C-130 aircraft during SHADE: 1. Solar spectrum, Journal of Geophysical Research, 108(D18), https://doi.org/10.1029/2002JD002687, 2003.

Haywood, J. M., Allan, R. P., Culverwell, I., Slingo, T., Milton, S., Edwards, J., and Clerbaux, N.: Can desert dust explain the outgoing long-wave radiation anomaly over the Sahara during July 2003?, Journal of Geophysical Research, 110, https://doi.org/10.1029/2004JD005232, 2005.

480 Heinold, B., Tegen, I., Schepanski, K., Tesche, M., Essenborn, M., Freudenthaler, V., Gross, S., Kandler, K., Knippertz, P., Müller, D., Schladitz, A., Toledano, C., Weinzierl, B., Ansmann, A., Althausen, D., Müller, T., Petzold, A., and Wiedensohler, A.: Regional modelling of Saharan dust and biomass-burning smoke. Part 1: Model description and evaluation, Tellus, 63B, 781–799, https://doi.org/10.1111/j.1600-0889.2011.00570.x, 2011.

Helmert, J., Heinold, B., Tegen, I., Hellmuth, O., and Wendisch, M.: On the direct and semidirect effects of Saharan dust over Europe: A
485   modeling study, Journal of Geophysical Research, 112, https://doi.org/10.1029/2006JD007444, 2007.

Hengl, T., de Jesus, J. M., Heuvelink, G. B. M., Gonzalez, M. R., Kilibarda, M., Blagotic, A., Shangguan, W., Wright, M. N., Geng, X., Bauer-Marschallinger, B., Guevara, M. A., Vargas, R., MacMillan, R. A., Batjes, N. H., Leenaars, J. G. B., Ribeiro, E., Wheeler, I., Mantel, S., and Kempen, B.: SoilGrids250m: Global gridded soil information based on machine learning, PLoS ONE, 12, https://doi.org/10.1371/journal.pone.0169748, 2017.

490 Hsu, N. C., Herman, J. R., and Weaver, C.: Determination of radiative forcing of Saharan dust using combined TOMS and ERBE data, Journal of Geophysical Research, 105, 20,649–20,661, https://doi.org/10.1029/2000JD900150, 2000.

Indoitu, R., Kozhoridze, G., Batyrbaeva, M., Vitkovskaya, I., Orlovsky, N., Blumberg, D., and Orlovsky, L.: Dust emission and environmental changes in the dried bottom of the Aral Sea, Aeolian Research, 17, 101–115, https://doi.org/10.1016/j.aeolia.2015.02.004, 2015.

Loeb, N. G., Priestley, K. J., Kratz, D. P., Geier, E. B., Green, R. N., Wielicki, B. A., O'Rawe Hinton, P., and Nola, S. K.: Determination of
495   Unfiltered Radiances from the Clouds and the Earth's Radiant Energy System Instrument, Journal of Applied Meteorology, 40, 822–835, https://doi.org/10.1175/1520-0450(2001)040<0822:DOURFT>2.0.CO;2, 2001.

Loeb, N. G., Manalo-Smith, N., Su, W., Shankar, M., and Thomas, S.: CERES Top-of-Atmosphere Earth Radiation Budget Climate Data Record: Accounting for in-Orbit Changes in Instrument Calibration, Remote Sensing, 8, https://doi.org/10.3390/rs8030182, 2016.

Löw, F., Navratil, P., Kotte, K., Schöler, H. F., and Bubenzer, O.: Remote-sensing-based analysis of landscape change in the desiccated
500   seabed of the Aral Sea- a potential tool for assessing the hazard degree of dust and salt storms, Environmentl Monitoring Assessments, 185, 8303–8319, https://doi.org/10.1007/s10661-013-3174-7, 2013.

Marticorena, B. and Bergametti, G.: Modeling the atmospheric dust cycle: 1. Design of a soil-derived dust emission scheme, Journal of Geophysical Research, 100, 16,415–16,430, 1995.

Meier, J., Tegen, I., Heinold, B., and Wolke, R.: Direct and semi-direct radiative effects of absorbing aerosols in Europe: Results from a
505   regional model, Geophysical Research Letters, 39, https://doi.org/10.1029/2012GL050994, 2012.

Micklin, P.: The past, present, and future Aral Sea, Lakes & Reservoirs: Research and Management, 15, 193–213, https://doi.org/10.1111/j.1440-1770.2010.00437.x, 2010.

Mie, G.: Beiträge zur Optik trüber Medien speziell kolloidaler Metallösungen, Ann. Phys., 330, 377–445, https://doi.org/10.1002/andp.19083300302, 1908.

510 Miinalainen, T., Kokkola, H., Lehtinen, K. E. J., and Kühn, T.: Comparing the Radiative Forcings of the Anthropogenic Aerosol Emissions From Chile and Mexico, Journal of Geophysical Research: Atmospheres, 126, https://doi.org/10.1029/2020JD033364, 2021.

Nobakht, M., Shahgedanova, M., and White, K.: New Inventory of Dust Emission Sources in Central Asia and Northwestern China Derived From MODIS Imagery Using Dust Enhancement Technique, Journal of Geophysical Research: Atmospheres, 126, https://doi.org/10.1029/2020JD033382, 2021.

515 O'Hara, S. L., Wiggs, G. F. S., Mamedov, B., Davidson, G., and Hubbard, R. B.: Exposure to airborne dust contaminated with pesticide in the Aral Sea region, The Lancet, 355, 627–628, https://doi.org/10.1016/S0140-6736(99)04753-4, 2000.

Pekel, J.-F., Cottam, A., Gorelick, N., and Belward, A. S.: High-resolution mapping of global surface water and its long-term changes, Nature, 540, 418–422, https://doi.org/10.1038/nature20584, 2016.

Poggio, L., de Sousa, L. M., Batjes, N. H., Heuvelink, G. B. M., Kempen, B., Ribeiro, E., and Rossiter, D.: SoilGrids 2.0: producing soil
520 information for the globe with quantified spatial uncertainty, SOIL, 7, 217–240, https://doi.org/10.5194/soil-7-217-2021, 2021.

Prigent, C., Jiménez, C., and Catherinot, J.: Comparison of satellite microwave backscattering (ASCAT) and visible/near-infrared reflectances (PARASOL) for the estimation of aeolian aerodynamic roughness length in arid and semi-arid regions, Atmospheric Measurement Techniques, 5, 2703–2712, https://doi.org/10.5194/amt-5-2703-2012, 2012.

Ritter, B. and Geleyn, J.-F.: A comprehensive radiation scheme for numerical weather prediction models with potential applications in climate
525 simulations, Monthly Weather Review, 120, 303–325, https://doi.org/10.1175/1520-0493(1992)120<0303:ACRSFN>2.0.CO;2, 1992.

Ryder, C. L., Highwood, E. J., Rosenberg, P. D., Trembath, J., Brooke, J. K., Bart, M., Dean, A., Crosier, J., Dorsey, J., Brindley, H., Banks, J., Marsham, J. H., McQuaid, J. B., Sodemann, H., and Washington, R.: Optical properties of Saharan dust aerosol and contribution from the coarse mode as measured during the Fennec 2011 aircraft campaign, Atmospheric Chemistry and Physics, 13, 303–325, https://doi.org/10.5194/acp-13-303-2013, 2013.

530 Schättler, U., Doms, G., and Schraff, C.: A description of the nonhydrostatic regional COSMO-model, Part VII: User's guide, Tech. rep., Deutscher Wetterdienst, Offenbach, Germany, http://www.cosmo-model.org/, 2014.

Sinyuk, A., Torres, O., and Dubovik, O.: Combined use of satellite and surface observations to infer the imaginary part of refractive index of Saharan dust, Geophysical Research Letters, 30, https://doi.org/10.1029/2002GL016189, 2003.

Sokolik, I. N. and Toon, O. B.: Incorporation of mineralogical composition into models of the radiative properties of mineral aerosol from
535 UV to IR wavelengths, Journal of Geophysical Research, 104, 9423–9444, https://doi.org/10.1029/1998JD200048, 1999.

Volz, F. E.: Infrared Optical Constants of Ammonium Sulfate, Sahara Dust, Volcanic Pumice, and Flyash, Applied Optics, 12, 564–568, https://doi.org/10.1364/AO.12.000564, 1973.

Wang, W., Samat, A., Abuduwaili, J., Ge, Y., De Maeyer, P., and Van de Voorde, T.: Temporal characterization of sand and dust storm activity and its climatic and terrestrial drivers in the Aral Sea region, Atmospheric Research, 275, https://doi.org/10.1016/j.atmosres.2022.106242,
540 2022.

Wielicki, B. A., Barkstrom, B. R., Harrison, E. F., Lee, R. B., Smith, G. L., and Cooper, J. E.: Clouds and the Earth's Radiant Energy System (CERES): An Earth Observing System Experiment, Bulletin of the American Meteorological Society, 77, 853–868, https://doi.org/10.1175/1520-0477(1996)077<0853:CATERE>2.0.CO;2, 1996.

Wiggs, G. F. S., O'Hara, S. L., Wegerdt, J., van der Meers, J., Small, I., and Hubbard, R.: The dynamics and characteristics of aeolian dust in
545   dryland Central Asia: possible impacts on human exposure and respiratory health in the Aral Sea basin, The Geographical Journal, 169,
142–157, https://doi.org/10.1111/1475-4959.04976, 2003.

Wolke, R., Schröder, W., Schrödner, R., and Renner, E.: Influence of grid resolution and meteorological forcing on simulated Eu-
ropean air quality: A sensitivity study with the modeling system COSMO-MUSCAT, Atmospheric Environment, 53, 110–130,
https://doi.org/10.1016/j.atmosenv.2012.02.085, 2012.